remote sensing

MDPI

Article

Radar Target Detection Within Nonhomogeneous Sea Clutter via MSP-MIG Detectors

Jiayi Chen, Xiaoqiang Hua *, Yongqiang Cheng, Hao Wu, Zheng Yang and Hongqiang Wang

College of Electronic Science and Technology, National University of Defense Technology, Changsha 410073, China

* Correspondence: huaxiaoqiang12@nudt.edu.cn or hxq712@yeah.net

Highlights

What are the main findings?

- Proposed a novel manifold subspace projection (MSP) method extending subspace decomposition to manifold space, demonstrating superior target–clutter separability.
- Developed three MSP-based matrix information geometry (MIG) detectors leveraging geometric measures and achieved enhanced target detection performance in nonhomogeneous sea clutter through Hermitian positive-definite matrix modeling and geometric mean covariance estimation.

What are the implications of the main findings?

- Provides an effective tool for target detection in nonhomogeneous environments, enabling more robust maritime target detection without relying on traditional statistical homogeneity assumptions.
- Further integrating information geometry theory with radar signal processing opens new avenues for developing advanced manifold-based detectors in complex environments.

Abstract

Subspace decomposition is a widely adopted approach for mitigating clutter interference in complex sea clutter scenarios. Based on the subspace decomposition principle, this paper expands the method to manifold space and presents a set of matrix information geometry (MIG) detectors with manifold subspace projection (MSP) for handling the target detection problem in nonhomogeneous sea clutter. According to the general method, the sample data are modeled as Hermitian positive-definite (HPD) matrices, and the clutter covariance matrix is estimated as the geometric mean of secondary HPD matrices. Through subspace projection, we map the HPD matrices onto a submanifold to enhance target–clutter separability. Three MSP-MIG detectors are put forward in line with different geometric measures. The experimental results show that our MSP-MIG detectors perform better than both traditional detectors and their non-MSP counterparts in nonhomogeneous sea clutter environment.

Keywords: target detection; matrix manifold; subspace projection; nonhomogeneous clutter

Check for updates

Academic Editor: Massimiliano Pieraccini

Received: 18 December 2025
Revised: 5 February 2026
Accepted: 7 February 2026
Published: 13 February 2026

Copyright: © 2026 by the authors. Licensee MDPI, Basel, Switzerland. This article is an open access article distributed under the terms and conditions of the Creative Commons Attribution (CC BY) license.

1. Introduction

Target detection in nonhomogeneous sea clutter has emerged as a significant challenge in the radar remote sensing area in recent years [1–4]. Over the past few decades, radar target detection has attracted considerable research attention, leading to the development

of numerous classical detectors [5–8]. Among these, constant false alarm rate (CFAR) detectors have been the most widely adopted [9]. CFAR is a fundamental radar signal processing technique designed to maintain a consistent false alarm probability when operating in environments with unknown noise and clutter power level [10]; the core principle of CFAR detectors involves dynamically adjusting detection thresholds through adaptive background power estimation [11]. For homogeneous Gaussian-distributed clutter environment, the cell average (CA)-CFAR [12] was originally developed. CA-CFAR uses mean reference window values for power estimation; however, it suffers from threshold overestimation and missed detection when strong interference exists in reference cells. This limitation led to the development of the smallest of (SO)-CFAR [13], which employs the smaller mean of leading or lagging reference windows to improve interference resilience. In [14], the greatest of (GO)-CFAR was created to address clutter-edge-induced false alarms by selecting the larger reference window mean. An illustration of CFAR detectors is shown in Figure 1. However, these traditional CFAR methods remain constrained by their reliance on local window estimation and perform poorly in complex nonhomogeneous environments. To overcome the problem, the adaptive matched filter (AMF) [15] was introduced; it utilized interference covariance matrix estimation to generate optimal weights that maximize the SINR for adaptive nonhomogeneous clutter suppression. In [16], the adaptive normalized matched filter (ANMF) was developed. ANMF incorporates an energy normalization process to enhance detection robustness and exhibits amplitude invariance. In [17], an adaptive matched filtering detector (NMAMF) based on the median power and the normalized sampling covariance matrix was developed to deal with nonhomogeneous sea clutter scenarios. For different backgrounds, some improved AMF methods have been proposed [18,19]. Nevertheless, both AMF and ANMF require sufficient training samples for accurate covariance matrix estimation, and the performance of these detectors remain constrained due to requirements for homogeneous sample data and vulnerability to heterogeneous interference [20–23].

Recent approaches have incorporated a priori clutter characteristics into detector design [24–30]. For instance, in [31], the authors proposed using topographic information to mitigate dynamic outliers in training data. In [32], the radar target detectors were designed based on Gamma or inverse Gamma-distributed texture components, and the speckle component followed an inverse Wishart distribution. Another example was given in [33], in which an adaptive Rao detector was designed to improve detection performance, leveraging a priori knowledge of sea clutter. Neural network-based radar target detection methods have also gradually become a research hotspot [34–36]. For instance, in [37], a detection method based on the Faster R-CNN structure was proposed. Based on various networks, different methods utilizing neural networks for target detection have been proposed [38]. These knowledge-aided methods exhibit significant performance enhancements, largely attributed to their capacity to utilize comprehensive clutter characteristics, and deep learning methods require prior data for learning and training [39–44]. However, such information is usually not easy to achieve in practical applications. Without adequate environmental information, severe performance degradation often occurs [45–47].

In recent years, the use of matrix information geometry (MIG) to tackle signal processing issues has drawn significant interest [48–56]. As an advanced extension of classical information geometry, MIG reviews the geometrical properties of probability distributions and their practical implementation and formulates the statistical manifold in information geometry theory through matrix representations [57]. Building upon this foundation, in [58], the authors developed a class of MIG detectors and demonstrated analytical excellence over existing detection methods. An illustration of MIG detectors is displayed in Figure 2. MIG detectors statistically model the original data as covariance matrices and

utilize the matrix manifold formed by these covariance matrices, thereby transforming the target detection problem into a discrimination task between targets and clutter on the manifold [59]. Due to differences in the statistical characteristics of targets and clutter, their regional distributions within the manifold space also differ. This enables the use of geometric distances in the manifold space to distinguish targets from clutter, ultimately achieving target detection. The key to the superior performance of the MIG detector lies in its ability to extract discriminative features between the target and clutter and effectively differentiate them within the high-dimensional manifold space [60]. By leveraging the intrinsic geometric structures of relevant manifolds, MIG detectors operate without requiring a priori knowledge of clutter characteristics. In [61], the authors further explain that the effects of MIG detectors are related to the discriminative ability of the geometric measurements used. However, the performance limitations of MIG detectors appear in nonhomogeneous marine environments, and target-disturbance separation becomes highly challenging.

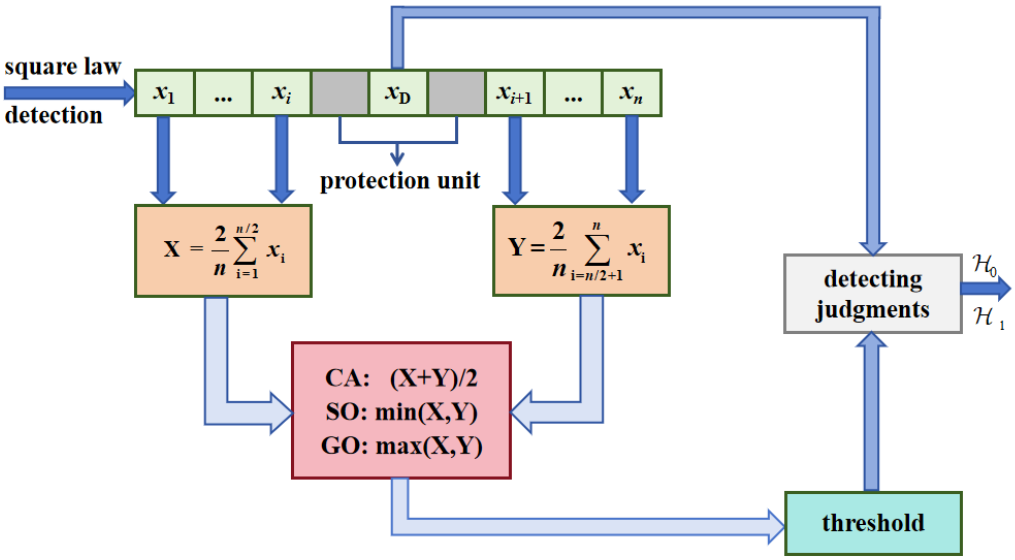


Figure 1. Illustration of CFAR detectors. **X** represents the mean of units x_1 to x_i, and **Y** represents the mean of units x_{i+1} to x_n.

To overcome the constraint, we propose a novel manifold subspace projection (MSP)-based MIG detectors. Our approach models the sample data in each cell as an Hermitian positive-definite (HPD) matrix and then applies singular value decomposition (SVD) [62–67] to derive optimal subspace projections. The clutter covariance matrices (CCMs) are estimated by geometric means. A projection is designed to map the HPD matrix manifold onto a submanifold with reduced clutter interference, thereby enhancing the separability between target and clutter. This MSP process improves signal-to-clutter ratio (SCR) and enhances detection performance. Experimental results confirm that our MSP-MIG detectors surpass both conventional approaches and baseline MIG detectors in nonhomogeneous sea clutter scenarios. The main contributions of this paper are summarized as follows:

- A novel MSP operation is proposed and integrated into the MIG detection paradigm. This operation effectively merges subspace projection theory with the geometric principles of MIG. By projecting high-dimensional manifold data onto a more discriminative low-dimensional submanifold, it deliberately increases the representational distance between the clutter and the target in the geometric space, thereby enhancing their separability.
- Three distinct MSP-MIG detectors are developed based on different geometric measures. The method models radar data as HPD matrices. An interference-suppressing

subspace projection operator is constructed to map the original manifold onto a lower-dimensional submanifold that preserves the intrinsic geometric structure. This process mitigates the impact of clutter nonhomogeneity while maintaining the inherent geometric relationships of the matrix manifold, directly addressing the performance limitations of conventional MIG detectors in nonhomogeneous sea clutter environments. In order to investigate the performance of MSP-MIG detectors with respect to different geometric measures, three typical geometric measures prevalent in MIG detection methods are selected, leading to the design of three classes of MSP-MIG detectors. Experimental verification confirms that each measure enables the MSP-MIG detectors to achieve consistently superior performance across diverse scenarios.

- The superior detection performance of the proposed MSP-MIG detectors is rigorously validated in nonhomogeneous sea clutter scenarios. Experimental results on real-world datasets demonstrate that, in typical nonhomogeneous sea clutter, the proposed detectors achieve significantly better detection probability and false alarm control compared to both traditional detectors and earlier MIG-based methods. This work provides a novel and effective coherent solution for radar target detection under complex sea conditions.

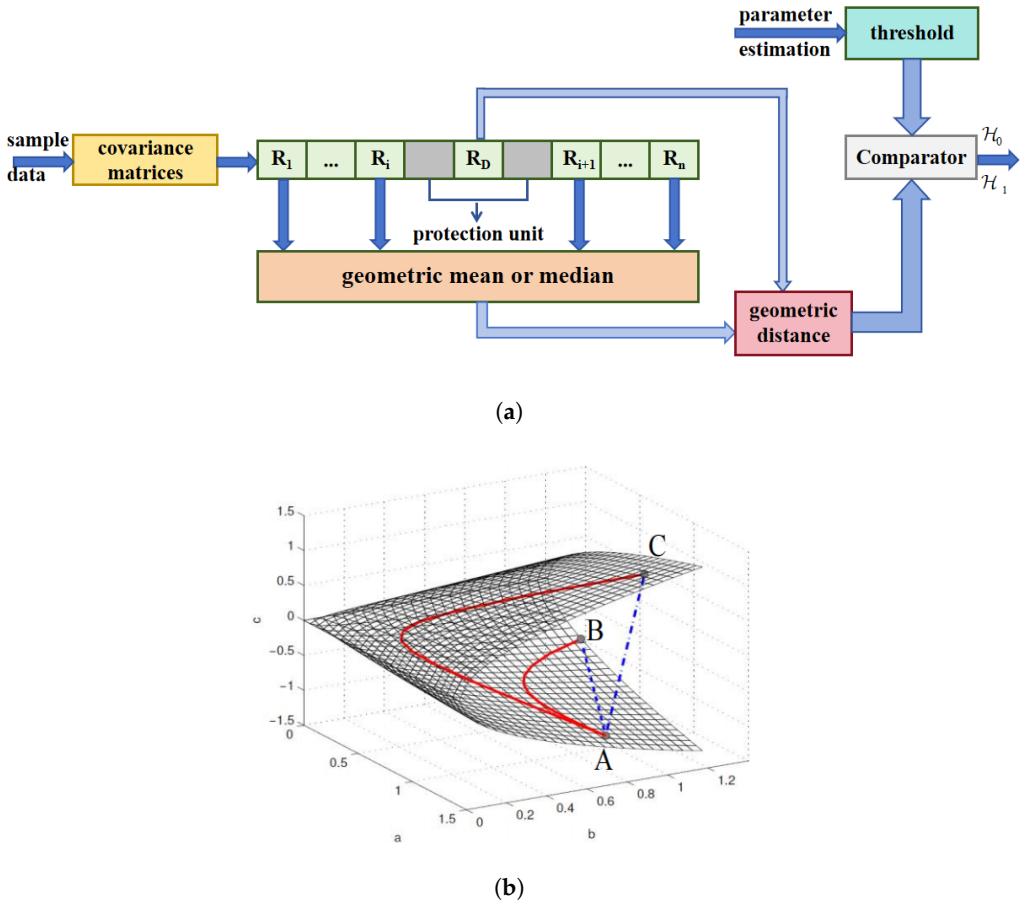


Figure 2. Illustration of MIG detectors: (**a**) detection principle; (**b**) measurement of the difference between two points on a matrix manifold [68]. $\{\mathbf{R}_i\}$ represents the HPD matrices.

MSP performs projection on the manifold formed by HPD matrices. For a cell under test, we utilize secondary data to estimate a local clutter centroid on the manifold. Subspace projection is executed within the tangent space at each point on the manifold. The tangent space is a Euclidean vector space that locally approximates the manifold. The dominant eigenvectors within this space define the directions of maximum local clutter variation.

Rather than performing linear subtraction in Euclidean space, MSP computes a projection along the geodesics of the manifold. The test point is projected away from the clutter subspace. This is mathematically formalized as minimizing the geodesic distance from the test point to a submanifold orthogonal to the dominant clutter directions. The detection statistic is then calculated as the geodesic distance on the projected submanifold. For a target, this distance is inherently larger than the original distance because the projection actively increases the separation between the clutter and target subspaces. This approach is theoretically better suited in nonhomogeneous clutter environments.

The remainder of this paper is arranged as follows. In Section 2, the methodology of MIG detectors is introduced. Section 3 details the framework of the proposed MSP-MIG detection method. Section 4 presents the experimental results, with the discussion in Section 5, and the work is concluded in Section 6.

2. Problem Formulation

Let $\boldsymbol{y} = [y_0, y_1, \ldots, y_{N-1}]^{\mathrm{T}}$ represent the sample data collected through N temporal stationary channels. Following standard formulation, the target detection problem can be expressed as a binary hypothesis test:

$$\begin{cases} \mathcal{H}_0 : \begin{cases} \boldsymbol{y} = \boldsymbol{c} \\ \boldsymbol{y}_k = \boldsymbol{c}_k, \quad k = 1, 2, \ldots, K, \end{cases} \\ \mathcal{H}_1 : \begin{cases} \boldsymbol{y} = \boldsymbol{s} + \boldsymbol{c} \\ \boldsymbol{y}_k = \boldsymbol{c}_k, \quad k = 1, 2, \ldots, K, \end{cases} \end{cases} \tag{1}$$

where $(\cdot)^{\mathrm{T}}$ represents the transpose, K denotes the number of reference cells, $\boldsymbol{y}$ and $\boldsymbol{y}_k$ represent the observed data, $\boldsymbol{c}$ and $\boldsymbol{c}_k$ correspond to clutter components, and the vector $\boldsymbol{s} = \alpha \boldsymbol{p}$ represents the target signal. Here, α is an unknown complex amplitude incorporating channel propagation effects and target radar cross-section (RCS), while $\boldsymbol{p}$ is the steering vector given by

$$\boldsymbol{p} = \frac{1}{\sqrt{N}} \left[1, \exp(-i2\pi f_d), \ldots, \exp(-i2\pi f_d (N-1)) \right]^{\mathrm{T}}, \tag{2}$$

where N denotes the number of pulses, and f_d denotes the normalized Doppler frequency.

Here, the null hypothesis $\mathcal{H}_0$ indicates target absence, while $\mathcal{H}_1$ represents the alternative hypothesis indicating the presence of the target signal.

The sample data are represented as an HPD matrix, encapsulating the energy or correlation of the sample data. Various matrix structures, including the Toeplitz matrices, the persymmetric covariance estimators, and the diagonal loading, can model the sample data. In this paper, we concentrate on the Toeplitz structure HPD matrix $\boldsymbol{R}$, which is given by

$$\boldsymbol{R} = \mathbb{E}\left[\boldsymbol{y}\boldsymbol{y}^{\mathrm{H}} \right] = \begin{bmatrix} r_0 & r_1^* & \cdots & r_{n-1}^* \\ r_1 & r_0 & \cdots & r_{n-2}^* \\ \vdots & \ddots & \ddots & \vdots \\ r_{n-1} & \cdots & r_1 & r_0 \end{bmatrix}, \tag{3}$$

where $\boldsymbol{y}$ denotes the sample data, $(\cdot)^{\mathrm{H}}$ represents the Hermitian transpose, $\mathbb{E}[\cdot]$ represents the statistical expectation, $(\cdot)^*$ denotes the conjugate, and r_k is the k–th correlation coefficient of $\boldsymbol{y}$, given by

$$r_k = \mathbb{E}\left[y_i y_{i+k}^* \right], \quad 0 \le k \le n-1, \quad 0 \le i \le n-1, \tag{4}$$

Based on the ergodic stationary Gaussian process, r_k can be estimated as the mean of the sample data:

$$\hat{r}_k = \frac{1}{n-k} \sum_{j=0}^{n-1-k} y_i y_{i+k}^*, \quad 0 \le k \le n-1, \tag{5}$$

Each HPD matrix $\boldsymbol{R}$ is a point on the manifold. The collection of all n × n HPD matrices forms a matrix manifold $\mathcal{P}$, expressed as:

$$\mathcal{P} = \left\{ \boldsymbol{R} \in \mathbb{C}(n), \boldsymbol{R}^{\mathrm{H}} = \boldsymbol{R}, \boldsymbol{R} \succ 0 \right\}, \tag{6}$$

where $\mathbb{C}(n)$ denotes the collection of n-dimensional complex covariance matrices.

According to the theory of MIG, the problem of target detection can be converted into a geometric problem on the matrix manifold. The presence or absence of the target can be determined by calculating the geometric distance between the HPD matrix of the cell under test and the estimated CCM of the reference cells, and then comparing it with the predefined threshold.

In our detection framework, we propose to derive a projection matrix $\boldsymbol{P}$ to facilitate efficient clutter reduction and feature extraction within a subspace. Through mapping the HPD matrices onto a clutter-reduced submanifold, the proposed method seeks to maximize the discriminability between target and clutter signatures while simultaneously minimizing informational redundancy, thereby significantly enhancing the target detection performance under sample-starved clutter conditions. Specifically, the projection matrix transforms the original manifold onto a clutter-reduced subspace, where any n × n HPD matrix $\boldsymbol{R}$ is mapped onto a more discriminative submanifold by

$$f(\boldsymbol{R}) = \boldsymbol{P}\boldsymbol{R}\boldsymbol{P}^{\mathrm{H}}, \tag{7}$$

This transformation projects the original manifold onto a subspace manifold, effectively reducing clutter interference and consequently enhancing the separability between the target and the clutter, thereby improving the detection performance. The corresponding detection decision is given by

$$d\left(\hat{\boldsymbol{R}}_{\perp}, f(\boldsymbol{R}_D)\right) \underset{\mathcal{H}_0}{\overset{\mathcal{H}_1}{\gtrless}} \gamma, \tag{8}$$

where $d(\cdot)$ denotes the geometric distance between two points on the matrix manifold, $\boldsymbol{R}_D$ denotes the HPD matrix of a cell under test, $\hat{\boldsymbol{R}}_{\perp}$ is the projection of the estimated CCM, calculated by the matrices of reference cells, and γ is the detection threshold.

The performance of the proposed method is related to geometric measures. This paper focuses on Kullback–Leibler divergence (KLD), symmetrized Kullback–Leibler divergence (SKLD), and Log-Euclidean metric (LEM), with detailed theoretical derivations and evidence in [58]. For two HPD matrices $\boldsymbol{X}, \boldsymbol{Y} \in \mathcal{P}$, the KLD, SKLD, and LEM are defined as follows:

$$\mathrm{KL}(\boldsymbol{X}, \boldsymbol{Y}) = \mathrm{tr}\left(\boldsymbol{X}^{-1}\boldsymbol{Y} - \log\left|\boldsymbol{X}^{-1}\boldsymbol{Y}\right| - \boldsymbol{I}\right), \tag{9}$$

where $\mathrm{tr}(\cdot)$ denotes the trace of a matrix, the symbol $|\cdot|$ denotes the determinant of a matrix, and $\boldsymbol{I}$ is the identity matrix.

$$\mathrm{SKL}(\boldsymbol{X}, \boldsymbol{Y}) = \frac{1}{2}\mathrm{tr}\left(\boldsymbol{X}^{-1}\boldsymbol{Y} + \boldsymbol{Y}^{-1}\boldsymbol{X} - 2\boldsymbol{I}\right), \tag{10}$$

$$\mathrm{LEM}(\boldsymbol{X}, \boldsymbol{Y}) = \| \log(\boldsymbol{X}) - \log(\boldsymbol{Y}) \|_{\mathrm{F}}, \tag{11}$$

where $\| \cdot \|_F$ denotes the Frobenius norm.

3. MSP-MIG Detectors

In this section, we describe the MSP-MIG detector. The MSP maps HPD matrices from the original manifold onto a more discriminative submanifold, where clutter interference is reduced by effectively decoupling the clutter subspace and the target subspace. We apply one distance and two divergences to measure HPD matrices into the MSP-MIG detector. The core novelty of the proposed approach lies in performing subspace analysis on the matrix manifold. An illustration of a MSP-MIG detector is displayed in Figure 3, and the flowchart of the proposed detector is illustrated in Figure 4. First, sample data are modeled as HPD matrices. Next, the projection matrix is calculated via SVD, followed by the execution of manifold subspace projection. Subsequently, the clutter covariance matrices are estimated using geometric measures on the manifold, and the geometric distance is computed on the projected submanifold. Finally, the calculated result is compared against an adaptive threshold to make the final hypothesis decision in Equation (8). The entire process systematically integrates statistical modeling, manifold geometry, and adaptive detection, enabling larger target–clutter discrimination.

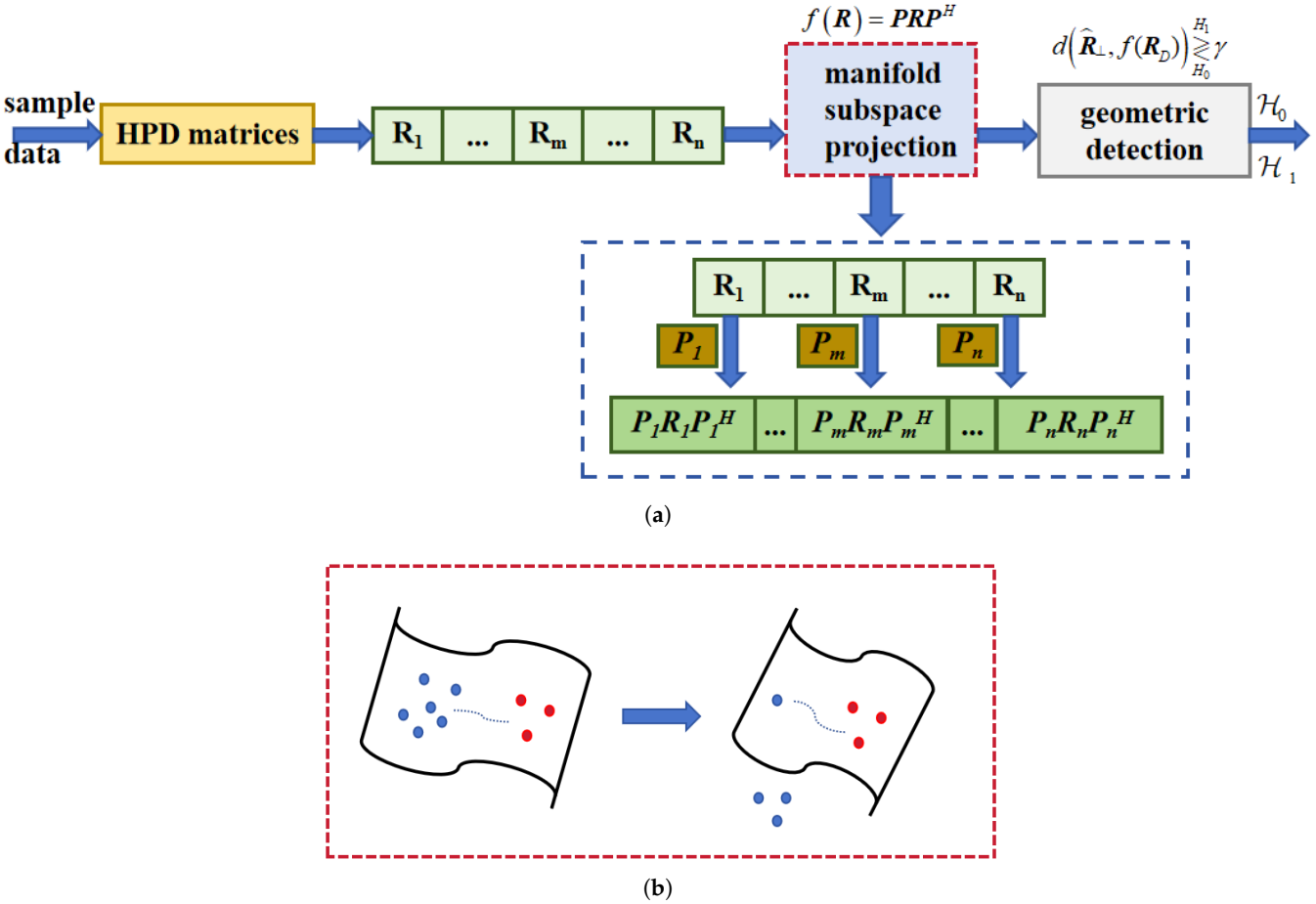


Figure 3. Illustration of an MSP-MIG detector: (**a**) flow diagram; (**b**) subspace manifold projection. The blue dots represent the clutter, and red dots represent the targets.

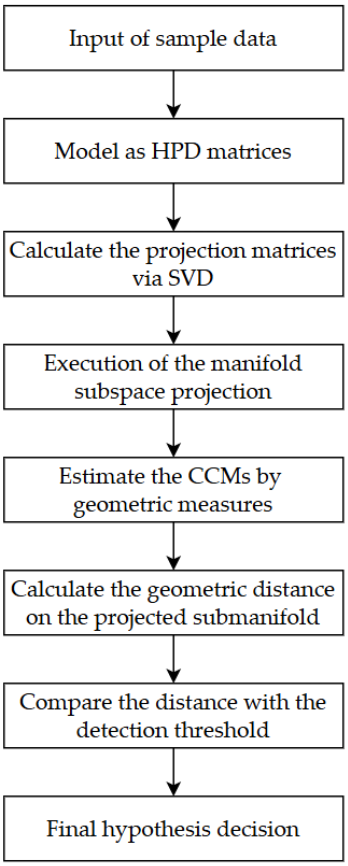


Figure 4. Flowchart of the MSP-MIG detector.

3.1. Geometric Mean for a Set of HPD Matrices

To enhance the discriminability between the target and the clutter, while minimizing informational redundancy, we use a projection that transforms the HPD matrices from the original manifold with lower discriminability to one with higher discriminability through subspace decomposition. The accuracy of subspace estimation profoundly influences overall performance, as it is essential to achieve a clear separation between the clutter subspace and the target subspace, thereby maximizing the discriminative divergence between the target and the clutter.

To achieve a more robust estimation of the clutter subspace, we employ geometric means to calculate the covariance matrices of sample data instead of the traditional mean, thereby significantly improving the robustness and reliability of the subspace estimation process.

As commonly known, the arithmetic mean of a set of positive real numbers $\{x_m\}$ is calculated by

$$\hat{x} = \frac{1}{M}\sum_{m=1}^{M} x_m, \quad m = 1, 2, \ldots, M, \tag{12}$$

where M is the number of data, and the arithmetic mean is the minimum value of the sum of squares:

$$\hat{x} = \arg\min_{x\in\mathbb{R}} \sum_{m=1}^{M} |x - x_m|^2, \quad m = 1, 2, \ldots, M, \tag{13}$$

where $\mathbb{R}$ is the set of all real numbers, and $|x - x_m|$ represents the distance between x and x_m.

Similarly, the geometric mean of a set of HPD matrices $\{\boldsymbol{R}_i\}$ is given by

$$\hat{\boldsymbol{R}} = \arg\min_{\boldsymbol{R}\in\mathcal{P}} \sum_{i=1}^{K} \frac{1}{K} d^2(\boldsymbol{R}_i, \boldsymbol{R}), \quad i = 1, 2, \ldots, K \tag{14}$$

where K denotes the number of covariance matrices, $\mathcal{P}$ denotes the set of HPD matrices, $d^2(\cdot)$ represents the geometric distance between two points on the matrix manifold, and $\boldsymbol{R}_i$ denotes the ith HPD matrix.

In this work, we adopt three distinct geometric means to enhance the accuracy of our estimation process. The KL, SKL, and LEM means are given by the following propositions:

Proposition 1. *The KL mean matrix of K HPD matrices is*

$$\hat{\boldsymbol{R}} = \left(\frac{1}{K} \sum_{i=1}^{K} \boldsymbol{R}_i^{-1} \right)^{-1}. \tag{15}$$

Proposition 2. *The SKL mean matrix of K HPD matrices is*

$$\hat{\boldsymbol{R}} = \boldsymbol{A}^{-1/2} \left(\boldsymbol{A}^{1/2} \boldsymbol{B} \boldsymbol{A}^{1/2} \right)^{1/2} \boldsymbol{A}^{-1/2}, \tag{16}$$

where

$$\boldsymbol{A} = \sum_{i=1}^{K} \boldsymbol{R}_i^{-1}, \quad \boldsymbol{B} = \sum_{i=1}^{K} \boldsymbol{R}_i. \tag{17}$$

Proposition 3. *The LEM mean matrix of K HPD matrices is*

$$\hat{\boldsymbol{R}} = exp\left(\frac{1}{K} \sum_{i=1}^{K} log(\boldsymbol{R}_i) \right). \tag{18}$$

Proof. The proofs of the three geometric measurements are given in [69]. □

3.2. Calculation of Projection Matrices

In this subsection, we introduce the calculation of projection matrices in the MSP method.

For the ith cell under test $\boldsymbol{y}_i$ from the sample data $\boldsymbol{y} = [y_0, y_1, \ldots, y_{N-1}]^{\mathrm{T}}$, the corresponding HPD matrix $\boldsymbol{R}_{Di}$ is given by (3), (4) and (5). Commonly, the sample data contain the signal data and the clutter data, thus $\boldsymbol{R}_{Di}$ can be expressed as

$$\boldsymbol{R}_{Di} = \mathbb{E}[\boldsymbol{y}_i \boldsymbol{y}_i^{\mathrm{H}}] = \boldsymbol{R}_{DSi} + \boldsymbol{R}_{DCi}, \tag{19}$$

where $\boldsymbol{R}_{DSi}$ and $\boldsymbol{R}_{DCi}$ denote the ith target matrix and the clutter HPD matrix respectively.

In MIG detectors, the CCM of the ith cell $\hat{\boldsymbol{R}_{mi}}$ is usually estimated by the geometric mean of m surrounding reference cells, given by (13). The covariance matrix $\boldsymbol{R}_i$ of the clutter and the target of the ith cell is given by

$$\boldsymbol{R}_i = \frac{\hat{\boldsymbol{R}_{mi}}}{|\eta_i|^{\lambda}}, \tag{20}$$

where λ is a constant coefficient, with its value usually between 1 and 2, and η_i denotes the correlation coefficient between the current cell under test $\boldsymbol{Y}_i$ and its mth reference cell $\boldsymbol{Y}_m$ and is calculated by

$$\eta_i = \frac{\boldsymbol{Y}_i^{\mathrm{H}} \boldsymbol{Y}_m}{\|\boldsymbol{Y}_i\| \|\boldsymbol{Y}_m\|}. \tag{21}$$

Subsequently, we perform SVD on $\boldsymbol{R}_i$ to obtain the clutter matrix and the target matrix:

$$\boldsymbol{R}_i = \boldsymbol{U}_i \Sigma_i \boldsymbol{V}_i^{\mathrm{H}} = \boldsymbol{U}_i \begin{bmatrix} \sigma_1 & & & & \\ & \ddots & & & \\ & & \sigma_\alpha & & \\ & & & \ddots & \\ & & & & \sigma_n \end{bmatrix} \boldsymbol{V}_i^{\mathrm{H}}, \tag{22}$$

where $\boldsymbol{U}_i$ is the left singular matrix, $\boldsymbol{V}_i$ is the right singular matrix, and Σ_i is the singular value matrix.

In nonhomogeneous sea clutter environments, the clutter energy is significantly higher than the target energy; thus, the largest α singular values can be identified as the clutter subspace. We nullify the remaining singular values and then construct a clutter projection matrix $\boldsymbol{P}_{Ri}$ that maps the original data onto the clutter subspace:

$$\boldsymbol{P}_{Ri} = \sum_{j=1}^{\alpha} u_j v_j^{\mathrm{H}}, 1 \le j \le \alpha. \tag{23}$$

Consequently, the clutter in the ith cell under test can be interpreted as the projection of the original signal onto the clutter subspace. The clutter subspace $\boldsymbol{U}_{Ri}$ is calculated by

$$\boldsymbol{U}_{Ri} = \boldsymbol{P}_{Ri} \boldsymbol{Y}_i. \tag{24}$$

The target projection matrix $\boldsymbol{P}_i$ can be expressed as

$$\boldsymbol{P}_i = \boldsymbol{I} - \boldsymbol{P}_{Ri}. \tag{25}$$

Through $\boldsymbol{P}_i$, we can map the original matrix to another matrix $\boldsymbol{R}_{Si}$ with less clutter interference:

$$\boldsymbol{R}_{Si} = \boldsymbol{P}_i \boldsymbol{R}_i \boldsymbol{P}_i^{\mathrm{H}}. \tag{26}$$

The corresponding target subspace $\boldsymbol{U}_{Si}$ is expressed as

$$\boldsymbol{U}_{Si} = \boldsymbol{P}_i \boldsymbol{Y}_i = (\boldsymbol{I} - \boldsymbol{P}_{Ri}) \boldsymbol{Y}_i. \tag{27}$$

For each cell under test, we calculate the projection matrix $\boldsymbol{P}_i$ and apply it to each original matrix $\boldsymbol{R}_i$. The set of all the matrices after projection forms the subspace manifold $\mathcal{P}_S$, expressed as

$$\mathcal{P}_S = \left\{ \boldsymbol{R}_{S_i} \in \mathbb{C}^{n \times n} \right\} = \left\{ \boldsymbol{P}_i \boldsymbol{R}_i \boldsymbol{P}_i^{\mathrm{H}} \in \mathbb{C}^{n \times n} \right\}. \tag{28}$$

Through the above procedures, we achieve the projection from the original manifold $\mathcal{P}$ onto the subspace manifold $\mathcal{P}_S$ with reduced clutter interference and enhanced separability between the target and the clutter. The detection decision of MSP-MIG detectors is shown in (7). Performing target detection based on this new manifold leads to SCR improvement, thereby enhancing the detection performance.

4. Experiment Results

The application of MSP enhances the discriminability between the target and the clutter, which allows for better target detection performance in nonhomogeneous sea clutter. In this section, experiments are presented to confirm the performance superiority of the detectors proposed. Both simulation and real data experiments were performed. The performance of MIG detectors with and without the MSP, as well as the conventional methods, were compared in our experiments.

4.1. Analysis of the Target–Clutter Distance

To validate the target–clutter differentiation improvement of the proposed MSP-MIG detector, we conducted simulation experiment to compare the target–clutter discrimination capability between MIG detectors with and without MSP. The simulation experiment adopted a data dimension of $N = 8$ and target Doppler frequency normalized to $f_d = 0.25$. The dataset comprised 2000 groups of data, each containing $K(K = N)$ clutter-dominated range cells and one target-embedded cell at 25 dB SCR. We employed the compound Gaussian distribution to simulate clutter, the texture component followed a Gamma distribution, the speckle component was modeled via the covariance matrix R, and the compound structure was derived through element-wise multiplication by Gamma random variables to simulate nonhomogeneous clutter environments. Three distance or divergence (KLD, SKLD, LEM) were employed to calculate the distance or divergence between a target-included HPD matrix and the CCMs, comparing scenarios with and without MSP. Figure 5 shows the target–clutter distance for different geometric measures.

As demonstrated in Figure 5, the blue dots stand for the target–clutter distance with the MSP operation, and the green dots represent the distance without MSP. Obviously, the target–clutter distance with MSP implementation significantly exceeds that without MSP. To provide a more intuitive comparison, we calculated the mean values of the three geometric measures with and without the MSP. In Figure 5, the red line represents the mean value with MSP, while the black line represents the mean value without MSP. The specific data are presented in Table 1. It should be noted that the mean values only reflect the relative magnitude of differences and solely indicate the clutter–target distance variation with and without MSP within the same geometric measure. They cannot be used to compare differences across the three distinct measures. The proposed MSP method increases the target–clutter distance with all geometric measures, confirming the improvement in discriminative capability between the clutter and the target. In particular, in the cases of KLD and SKLD, the target–clutter distances exhibit similar patterns with high dispersion, whereas a more concentrated distribution is observed under the LEM.

Table 1. Mean values of clutter–target distance with and without MSP.

Mean Value of	KLD	SKLD	LEM
with MSP	47.96	75.54	28.99
without MSP	28.99	33.07	10.89

Figures 6–8 shows the clutter–target distance and the clutter–clutter distance for different geometric measures with and without MSP. The blue dots stand for the target–clutter distance, and the black dots represent the clutter–clutter distance. As can be seen from the figures, while the clutter–clutter distance shows almost no variation, the vertical coordinate values of the points representing clutter–target distances with MSP are greater than those of the points without MSP. Compared to conventional MIG detectors, the MSP-MIG detector demonstrates greater dispersion in target–clutter distance, indicating enhanced separability between the target and the clutter. The MSP improves the discriminative capability, which effectively increases the detection performance.

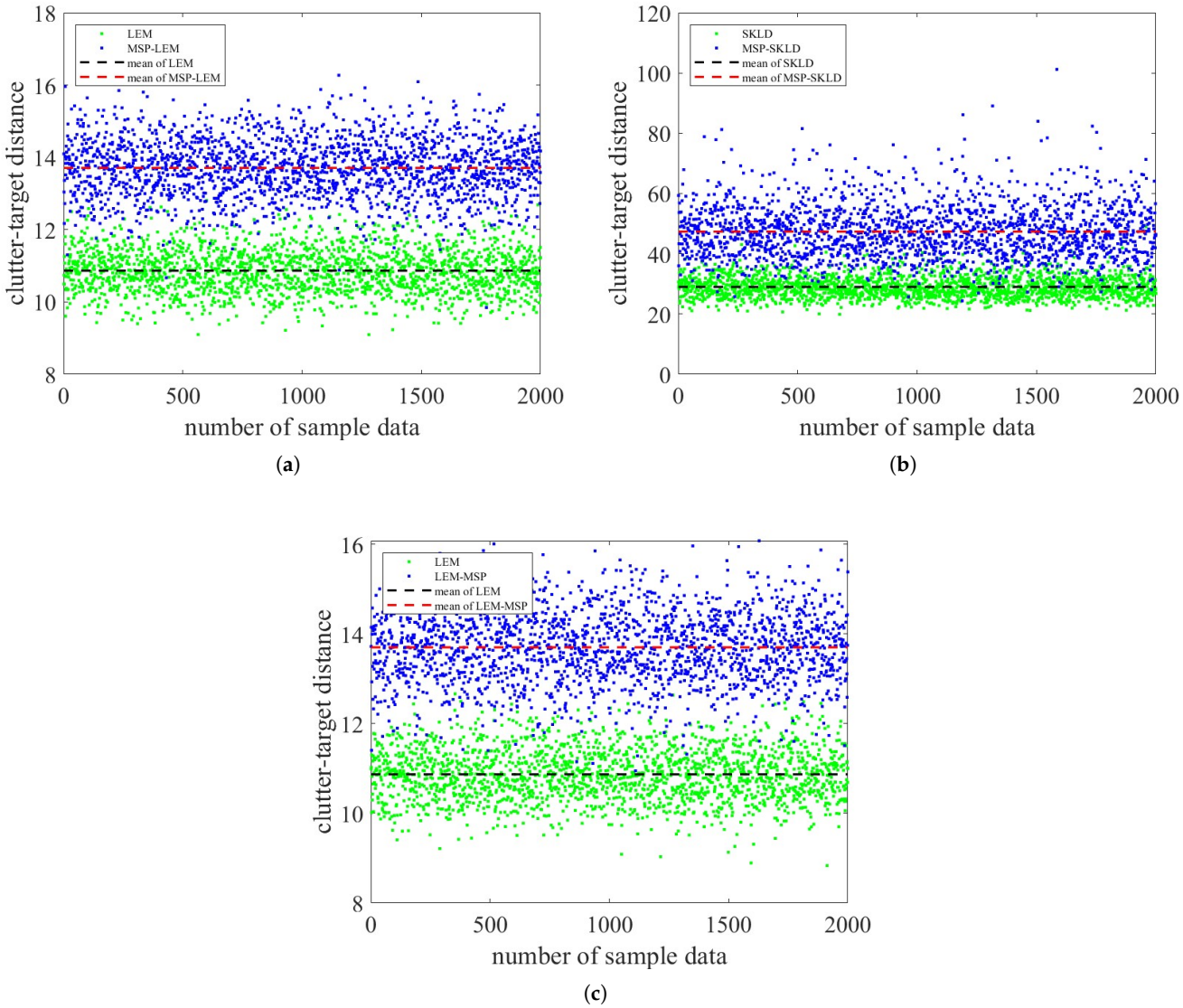


Figure 5. Clutter–target distance for different measures: (**a**) clutter–target distance of KLD; (**b**) clutter–target distance of SKLD; (**c**) clutter–target distance of LEM.

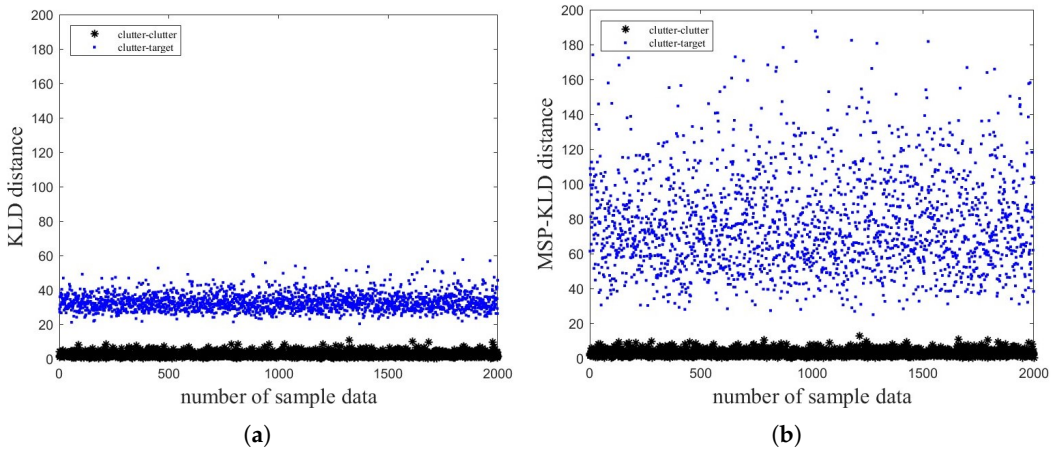


Figure 6. Clutter–target and clutter–clutter distance for KLD: (**a**) KLD; (**b**) MSP-KLD.

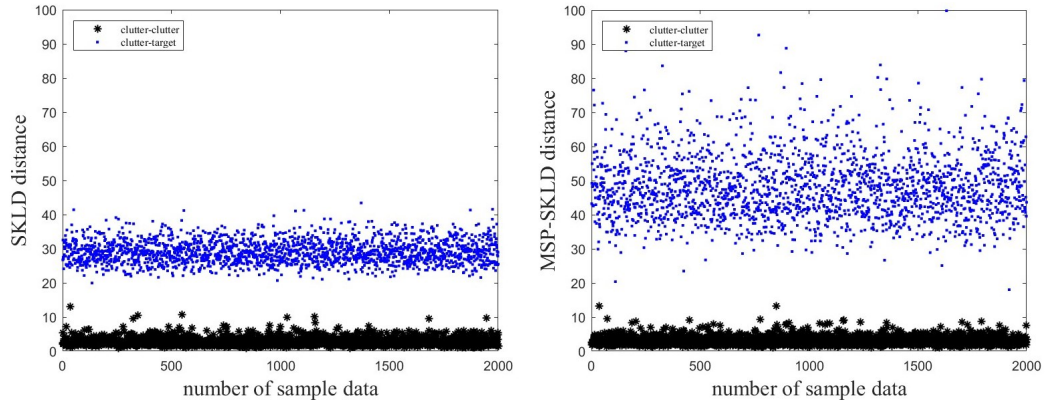


Figure 7. Clutter–target and clutter–clutter distance for SKLD: (**a**) SKLD; (**b**) MSP-SKLD.

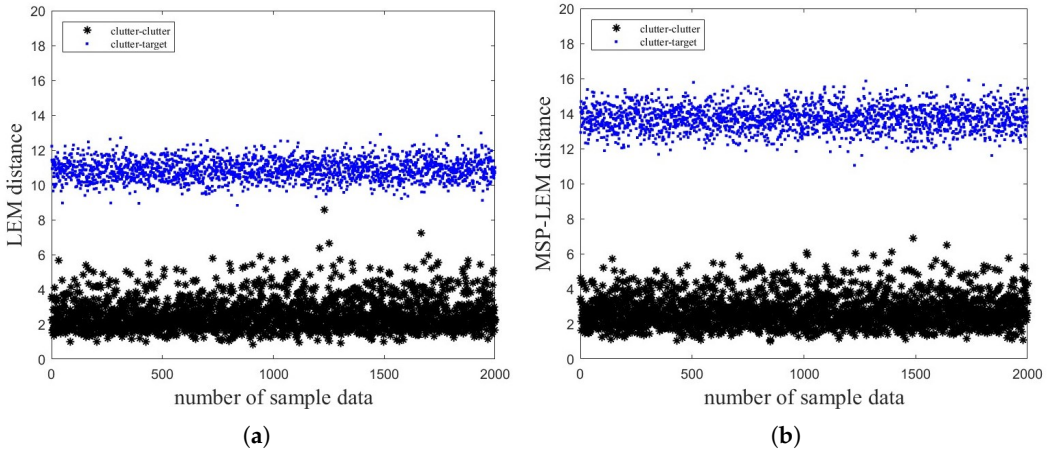


Figure 8. Clutter–target and clutter–clutter distance for LEM: (**a**) LEM; (**b**) MSP-LEM.

4.2. Analysis of Detection Probability

In this subsection, we present experiments on real data to further validate the performance of the proposed MSP method. We used one dataset from the IPIX radar and two datasets from the Sea-Detecting Radar Data-Sharing Program (SDRDSP).

4.2.1. Preliminary Experiment

The dataset "20191012112446_01_staring" obtained from SDRDSP was used in our preliminary experiment [70]. This dataset was collected at a marine target detection test site located in the Yatai coastal area of Shandong Province, China. An X-band solid-state power amplifier surveillance/navigation radar system was used for data collection. It worked in staring mode for around 3.33 s (which is equal to 10,000 pulses) and in HH polarization mode. The sea clutter dataset does not have any cooperative vessel targets. There are 5250 range cells in the fast-time dimension and 10,000 pulses in the slow-time dimension. We extracted 1–200 range cells and 1–8 pulses and injected a simulated moving target with a normalized Doppler frequency $f_d = 0.15$ and $SCR = 10$ dB at the 100th range cell. Figure 9 presents the experimental results.

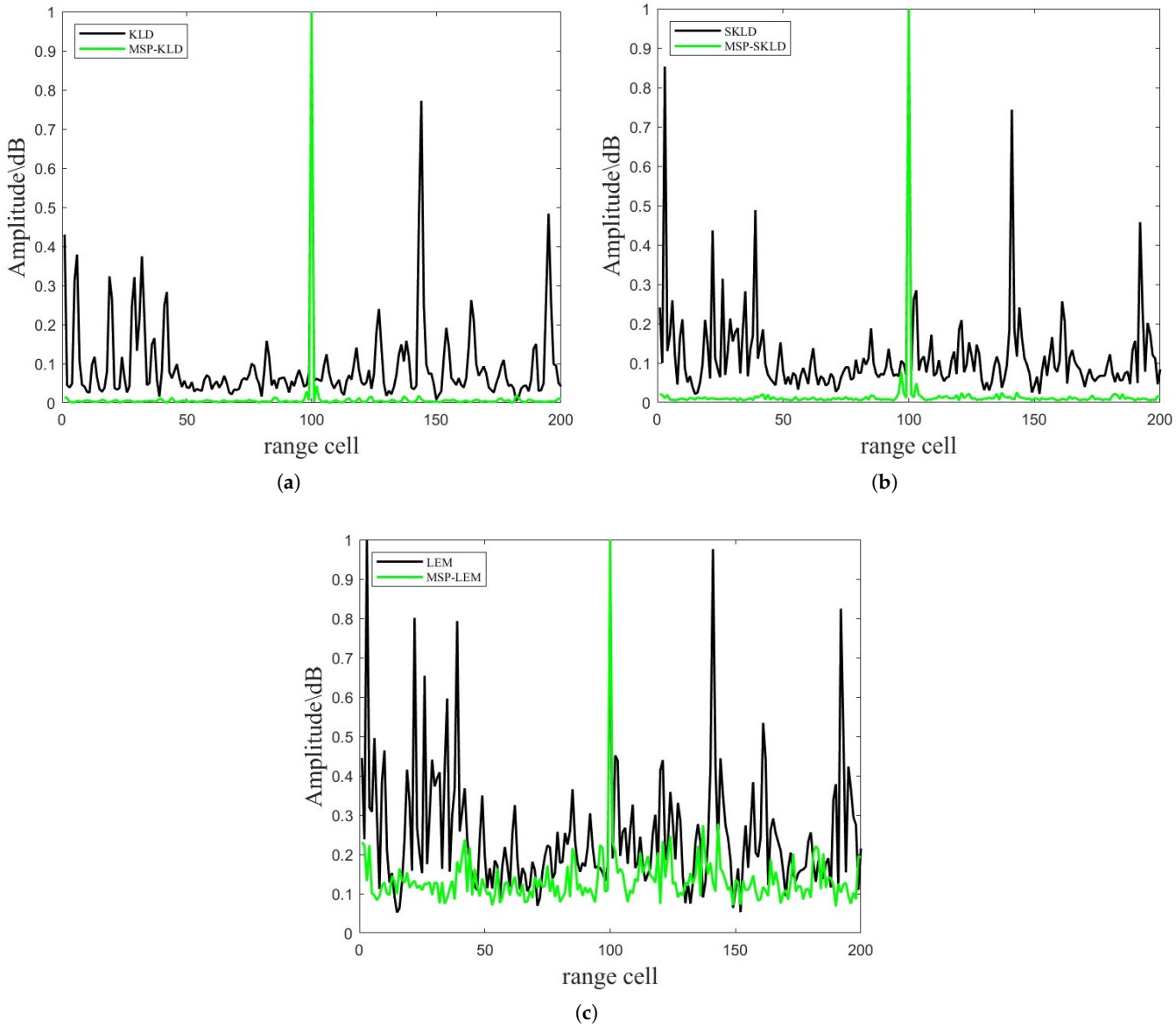


Figure 9. One-dimensional range profiles: (**a**) KLD result; (**b**) SKLD result; (**c**) LEM result.

In the picture, the horizontal coordinates are the range cells, the vertical coordinates are the normalized amplitudes, and the red lines represent the processing outcomes with MSP, while the black lines stand for results without MSP. The results presented correspond to one-dimensional range profiles. In KLD, SKLD and LEM, the results with MSP were significantly better than that without MSP. Among the three measures, KLD and SKLD achieved better performance than LEM.

4.2.2. Real Data of IPIX Radar

The experimental data used in the real-data experiment were collected in 1998 by the McMaster University IPIX radar, which is situated on the shores of Lake Ontario in Grimsby, Canada. Only sea clutter is included in the dataset "19980205_190524_ANTSTEP.cdf", which was employed to assess target detection performance [71]. The data are made up of 28 range cells in the fast-time dimension and 60,000 pulses in the slow-time dimension, having a pulse repetition frequency of 1000 Hz and multiple polarizations. Only the horizontal polarization results are reported in this work. A synthetic target signal with a normalized Doppler frequency $f_d = 0.15$ was injected into the clutter. The sample

dimension was fixed at $N = 8$, and the dataset was divided into 7500 segments along the slow-time dimension. The detection threshold was derived from the first 6300 segments, and the predefined false alarm probability was set to $P_f = 10^{-3}$. Detection probability was estimated via 4000 Monte Carlo simulations to ensure statistical reliability. Three geometric measures, KLD, SKLD and LEM, were employed in the performance comparisons of the proposed detectors. Detection was performed on two secondary data sizes: $K = N$ and $K = 2N$. The SCR was set from 0 dB to 30 dB.

Figures 10–12 depict the probability of detection Pd versus SCR curves for the MSP-MIG detectors based on KLD, SKLD, and LEM, alongside comparisons with their counterparts. Another comparison method is the total log-determinant divergence median (TLDM), which uses the TL divergence median to measure the distance between the cell under test and the clutter covariance matrix [72]. It is also a target detection method based on information geometry theory. We also included the traditional subspace decomposition method as a baseline in the experiments, represented by the curve labeled "SVD" in the figures. Specifically, on the basis of the CFAR target detection method, we incorporated a subspace decomposition preprocessing step based on singular values to compare the performance between the MSP and the traditional subspace decomposition method. At the same SNR, the detection probability of the MSP-MIG detectors was always higher than that of the other two detectors. When $K = 2N$, the detection performance surpassed $K = N$, and the advantages of MSP-MIG detectors were further increased. The MSP-MIG detectors exhibited robust performance even when other detectors performed poorly, except MSP-SKLD and MSP-LEM when $K = 2N$. This was probably because SKLD and LEM were not suitable in the environment. However, MSP-SKLD still performed better than other detectors when $K = N$. Notably, all MSP-MIG detectors outperformed their unprojected counterparts, demonstrating the effectiveness of MSP in enhancing the discrimination of the clutter and the target. The curve of Pd versus SCR of three measures is displayed in Figure 13. At both $K = N$ and $K = 2N$, the MSP-KLD MIG detector achieved the best performance, followed by the MSP-SKLD, and the MSP-LEM detector performed worse, since the MSP-KLD achieved the largest Pd at the same SCR.

However, identifying a universally superior detector remains challenging, as detection performance is highly dependent on the characteristics of the clutter. Future research efforts should prioritize the development of optimal detectors tailored to specific clutter types.

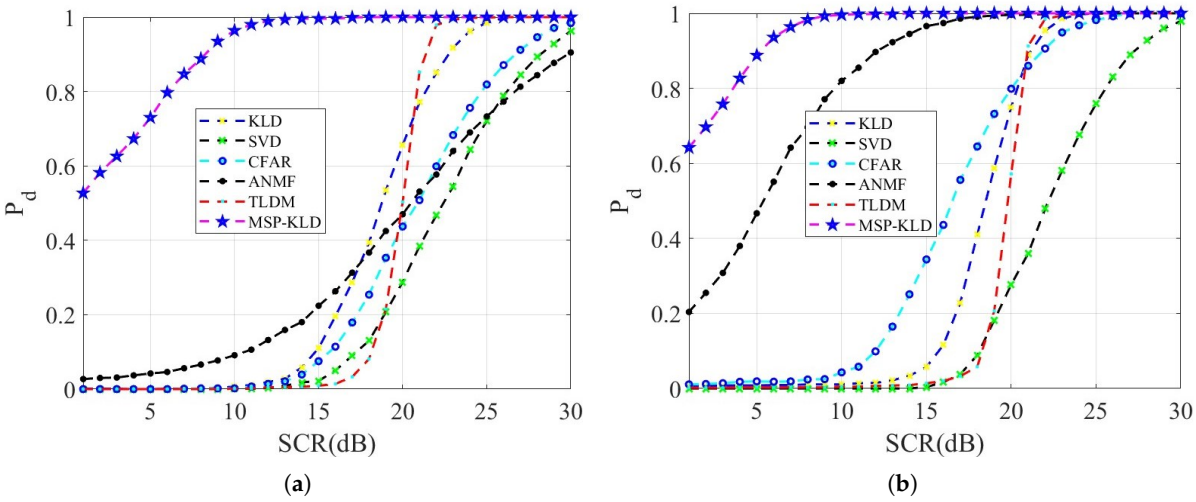


Figure 10. Pd vs. SCR for KLD: (**a**) $K = N$; (**b**) $K = 2N$.

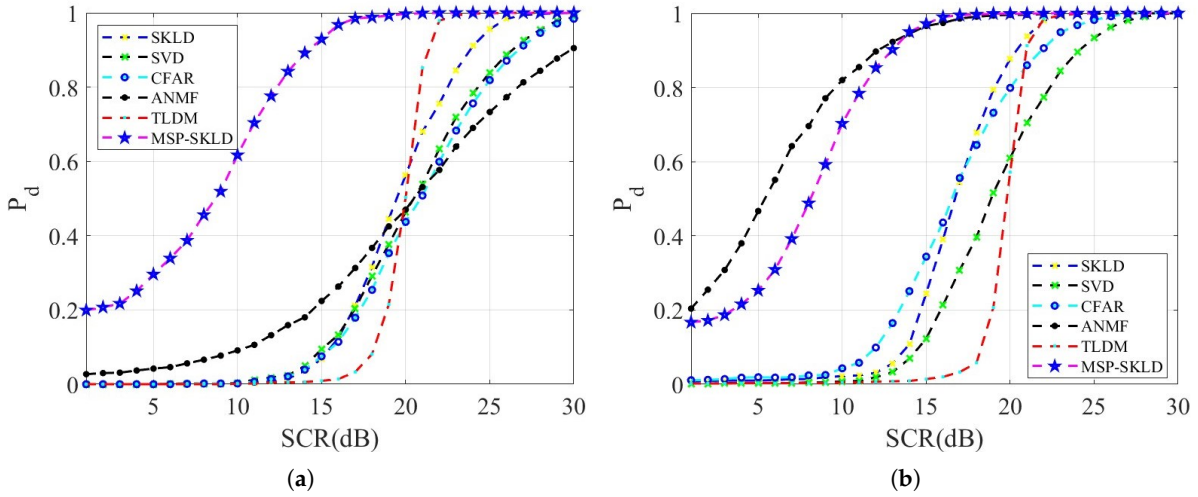


Figure 11. Pd vs. SCR for SKLD: (**a**) $K = N$; (**b**) $K = 2N$.

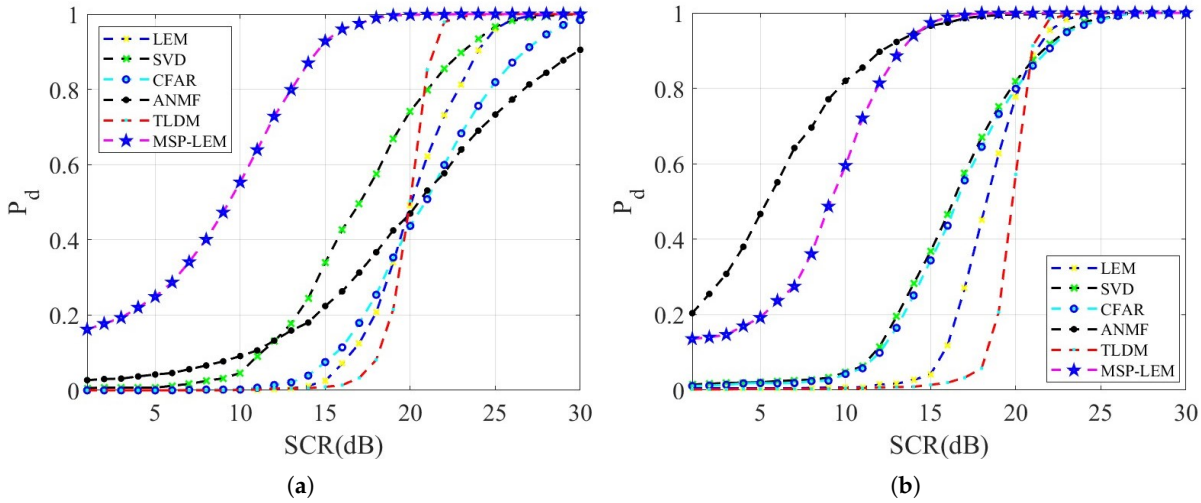


Figure 12. Pd vs. SCR for LEM: (**a**) $K = N$; (**b**) $K = 2N$.

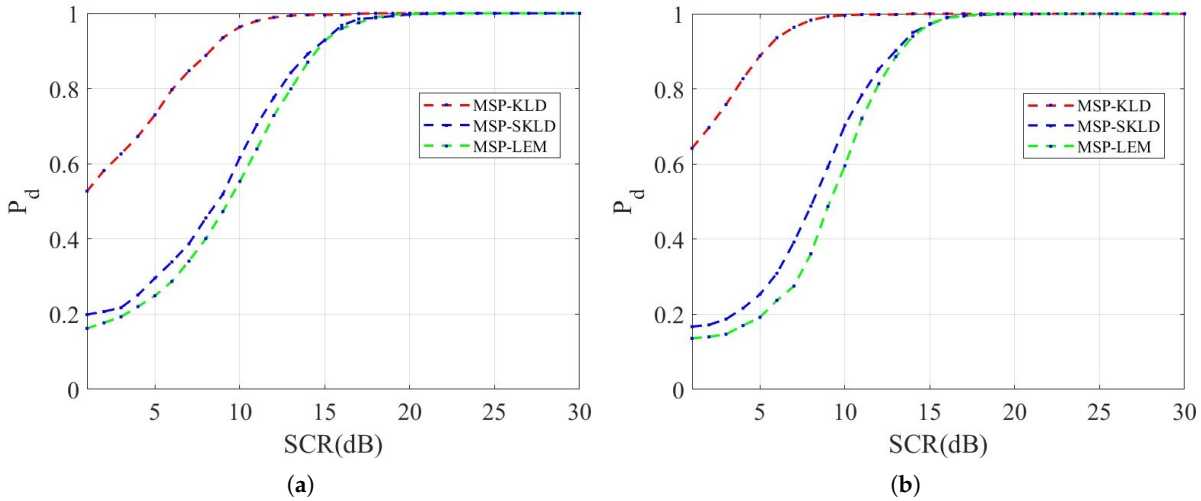


Figure 13. Pd vs. SCR for KLD, SKLD and LEM: (**a**) $K = N$; (**b**) $K = 2N$.

4.2.3. Real Data from the SDRDSP

This work additionally employed a set of experimental data from the SDRDSP. We used the dataset "20221112150043_stare_HH.mat" collected in 2022, with the data collection

radar situating on the shores of Yantai First Bathing Beach [73]. During the collection of that dataset, the sea state was level 4 with a wave height of 1.8 m. The original dataset contains 950 range cells (fast-time dimension) and 131,072 pulses (slow-time dimension), and we selected 28 range cells and 60,000 pulses for our experimental analysis. The radar operated at a pulse repetition frequency of 2000 Hz with multiple polarizations. A moving target with normalized Doppler frequency $f_d = 0.15$ was synthetically injected into the clutter.

With the sample data dimension fixed at $N = 8$, the dataset was partitioned into 7500 segments along the slow-time dimension. Detection performance was evaluated through the Pd versus SCR curves shown in Figures 14–16. Comparative analysis was based on three geometric measures, KLD, SKLD, LEM, and across two secondary data sizes, $K = N$ and $K = 2N$. The proposed MSP-MIG detectors demonstrated superior performance to both SVD, CFAR, TLDM and ANMF methods and their non-MSP counterparts. As shown in Figure 17, the MSP-KLD and the MSP-SKLD exhibited comparable performance, both outperformed MSP-LEM at $K = N$, and the MSP-KLD detector achieved optimal performance among the three measures, with notable performance advantage at $K = 2N$.

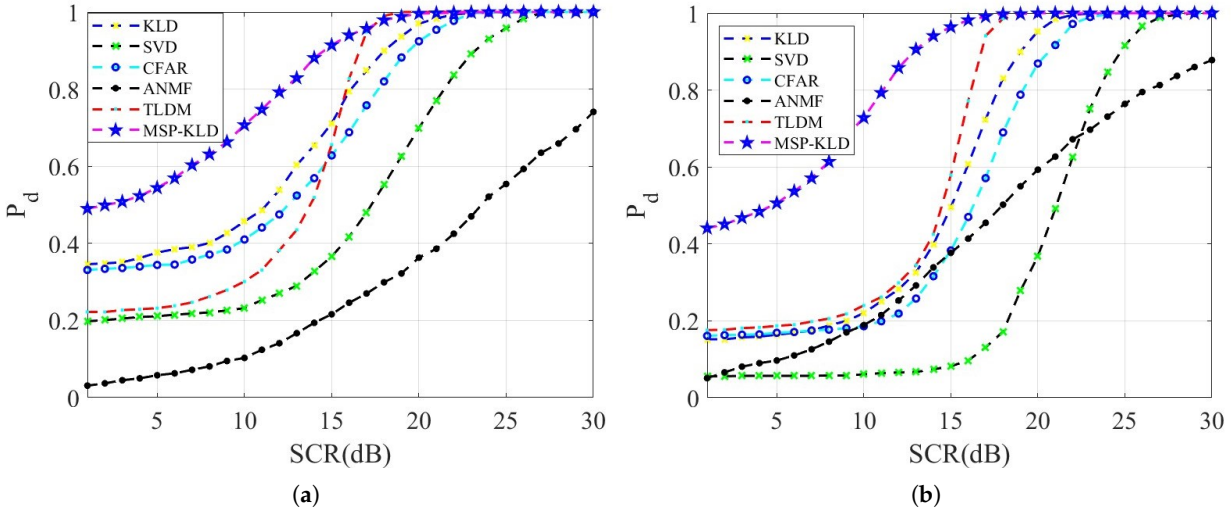


Figure 14. Pd vs. SCR for KLD: (**a**) $K = N$; (**b**) $K = 2N$.

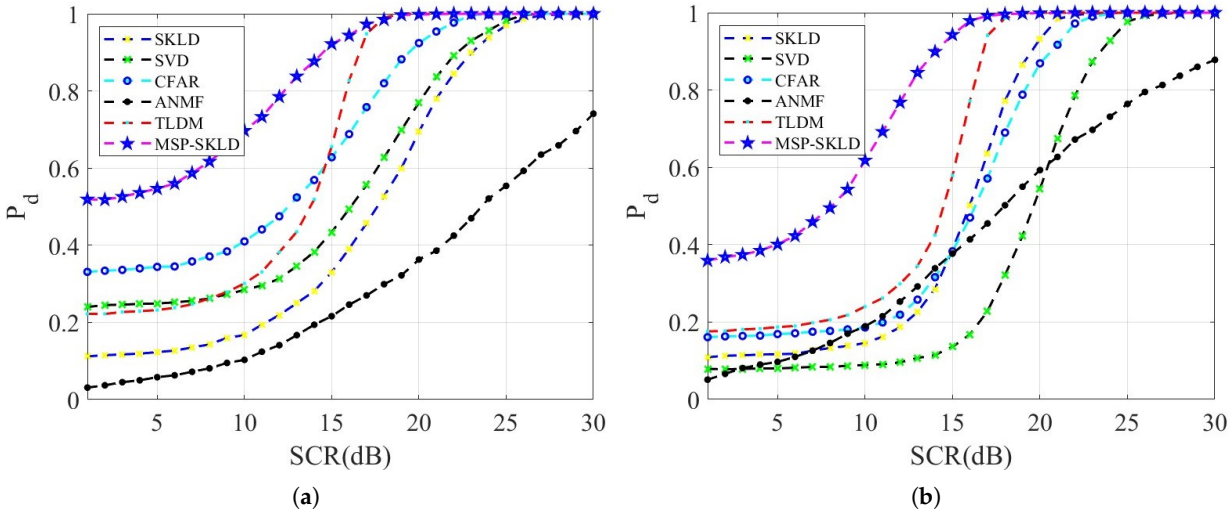


Figure 15. Pd vs. SCR for SKLD: (**a**) $K = N$; (**b**) $K = 2N$.

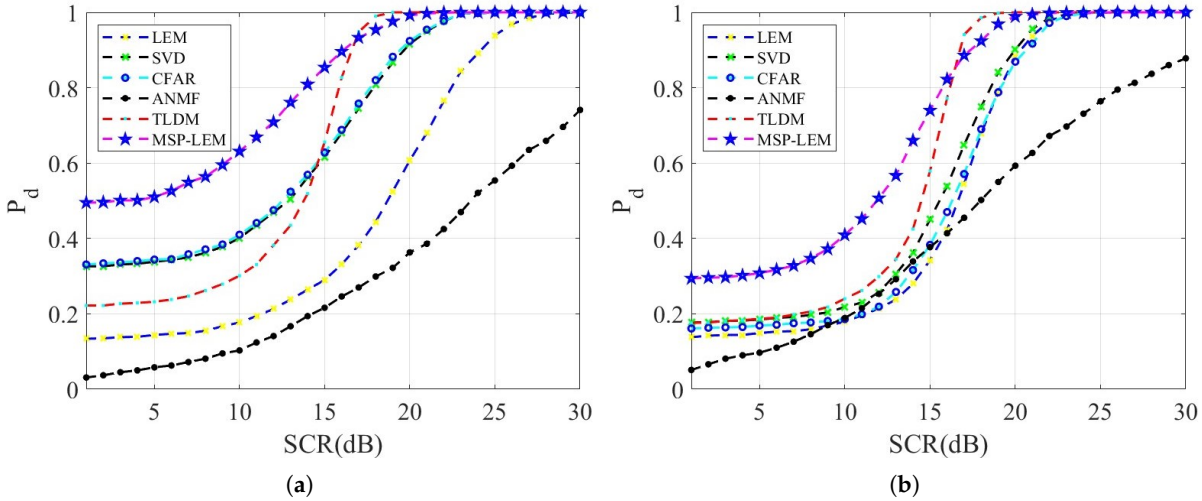


Figure 16. Pd vs. SCR for LEM: (**a**) $K = N$; (**b**) $K = 2N$.

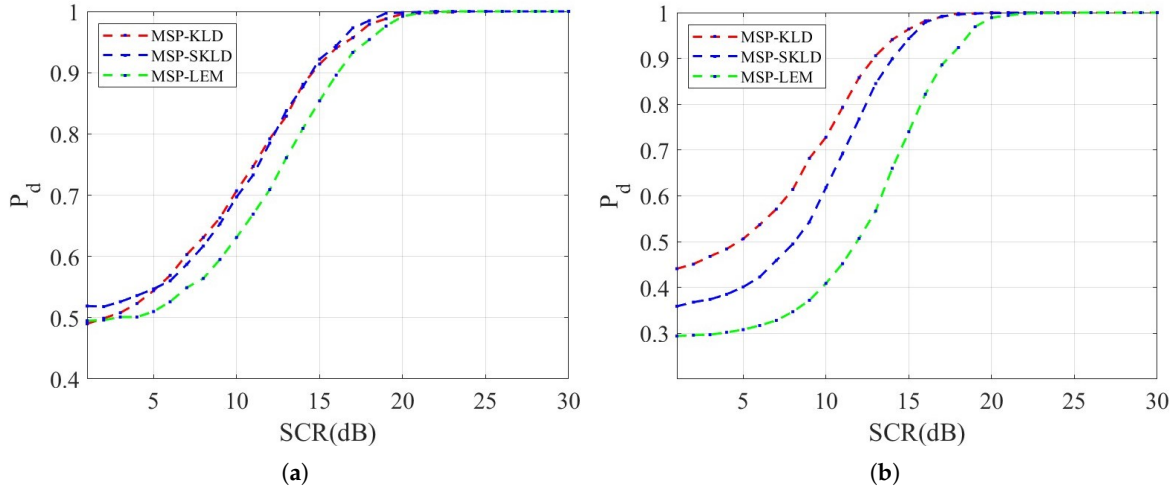


Figure 17. Pd vs. SCR for KLD, SKLD and LEM: (**a**) $K = N$; (**b**) $K = 2N$.

The experimental results from the two real-data experiments demonstrate that the MSP-MIG detector outperforms both conventional detectors and previous MIG detectors. However, it should be noted that different measurement approaches need to be considered for different scenarios, as there exists no universally applicable metric.

5. Discussion

In this section, we first discuss the effect of metrics. We employed three geometric divergences or distances in our experiments: KLD, SKLD, LEM. The MIG detectors displayed varying detection performance with different metrics. Then, we investigate the impact of the sizes of secondary data K. We compare the detection performance under two scenarios: $K = N$ and $K = 2N$. Finally, we summarize the strengths and weaknesses of the proposed method.

5.1. The Effect of Geometric Measures

In our experiments, we adopted two sets of real data: the dataset of IPIX radar collected by the McMaster University team in 1998 and the maritime detection dataset published in the Journal of Radars in 2022. Different geometric measures showed distinct detection performance when applied to the two datasets.

In the IPIX data, regardless of whether $K = N$ or $K = 2N$, KLD achieved the highest detection probability at the same SCR, indicating its superior performance in this regime. KLD demonstrated significant advantages over the other two geometric measures, and SKLD demonstrated a slight performance advantage over LEM. Across all SCR levels, LEM consistently yielded the lowest detection probability. In the SDRDSP data, at $K = N$, when the SCR was below five or above 15, SKLD outperformed both KLD and LEM, and for SCR between five and 15, KLD showed slightly better performance than SKLD, while LEM performed the worst across all SCR levels. When $K = 2N$, at the same SCR, KLD exhibited the best performance, and LEM performed the worst.

The performance differences of KLD, SKLD, and LEM on different datasets stem from their distinct approaches to measuring probability distribution divergence and inherent sensitivity to data characteristics. KLD is an asymmetric metric and quantifies information loss between the true and estimated distributions; it excels in high-SNR environments, such as the IPIX data. SKLD addresses the directional bias of KLD through symmetrization but underperforms with strongly asymmetric distributions. LEM employs Riemannian manifold-based linear mapping of covariance matrices, proving optimal for non-Gaussian clutter. Different metrics are suitable for different application scenarios and should be selected in specific environments. In the future, adaptive measure selection rather than manual experimentation represents a promising research direction.

5.2. The Effect of Sizes of Secondary Data

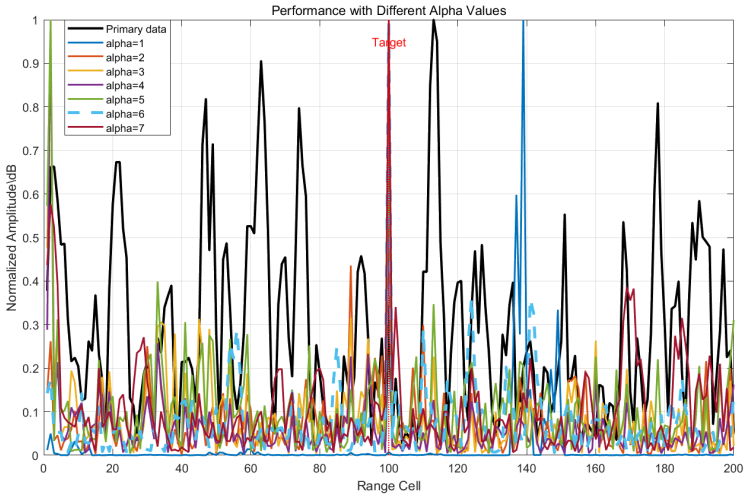
In the experiments, the sample data dimension was fixed at $N = 8$, with two configurations of secondary data size K, where $K = N$ and $K = 2N$. The distinction between $K = N$ and $K = 2N$ reflects the ratio between secondary data and the dimension of the sample data. For $K = N$, the secondary data equal the sample data dimension, providing only the minimum theoretical sample requirement for basic covariance matrix estimation. Conversely, the $K = 2N$ configuration offers doubled secondary data relative to the sample data dimension, yielding significantly enhanced covariance matrix estimation accuracy.

In the two real-data experiments, conventional CFAR and ANMF detectors, as well as the MIG detectors without MSP, all demonstrated better performance at $K = 2N$ than $K = N$. This improvement was particularly notable for AMF and ANMF. They performed poorly at $K = N$ but showed marked improvement at $K = 2N$, as their detection performance was highly sensitive to covariance matrix estimation. In comparison, the proposed MSP-MIG detectors showed excellent detection performance at both $K = N$ and $K = 2N$. This indicates that the proposed method maintains robust detection performance even under limited secondary data conditions.

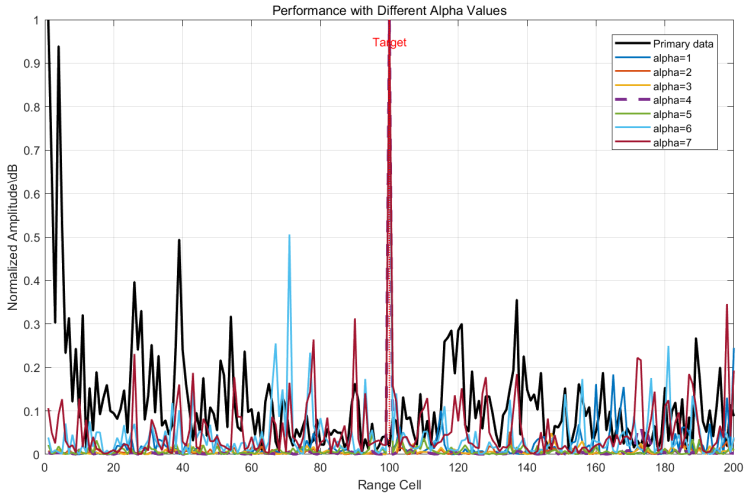
All the experiments were conducted in nonhomogeneous clutter environments. The results demonstrate that MSP can effectively increase the separation between the target and the clutter, thereby improving the SCR and achieving good detection performance in nonhomogeneous clutter. However, MSP also increases the computational complexity, and the performance of the proposed method in other diverse scenarios remains to be explored. For practical application, how to reduce the calculated complexity should be further considered. We also need to research whether universal applicability of our method across different scenarios can be achieved.

5.3. The Impact of Subspace Dimension α

We conducted two sets of experiments to explore the impact of subspace dimension α on detection performance. We used the datasets in Section 4.2.2 and Section 4.2.3 respectively, adopted the parameters in Section 4.2.1, and generated range-cell-normalized Doppler amplitude figures for α values ranging from one to seven, as shown in Figure 18.



(**a**)



(**b**)

Figure 18. Performance with different α values: (**a**) dataset "19980205_190524_ANTSTEP.cdf"; (**b**) dataset "20221112150043_stare_HH.mat".

For analysis, we selected eight pulses in fast-time dimension and 100 range cells in slow-time dimension, forming an experimental data matrix of dimensions 8 × 100. To quantitatively assess detection performance, a simulated target signal with a normalized Doppler frequency of $f_d = 0.15$ and an SCR of 5 dB was artificially injected at the 50th range cell. The experiment aimed to investigate the impact of the truncation order α in the MSP on detection performance. By systematically varying α from one to seven, we altered the number of principal components retained in the MSP step, thereby studying the influence of subspace dimension.

To evaluate the optimal value of α, we introduced several parameters detailed in Tables 2 and 3. Target response was the value at the target position, clutter suppression was calculated by the mean value excluding target region, and the T-C improvement was computed by the ratio of target response to clutter mean. The results showed that the optimal value of α varied across different datasets; the best α for dataset "19980205_190524_ANTSTEP.cdf" was six, while the best α for dataset "20221112150043_stare_HH.mat" was four. Since α represents the subspace dimension, its value is generally related to clutter intensity. Therefore, the selection of α needs to

be specifically considered for different scenarios. How to achieve adaptive α selection in varying environments is also a question worth considering.

Table 2. Dataset "19980205_190524_ANTSTEP.cdf".

α	Target Response	Clutter Suppression	T-C Improvement
1	0.007	0.0197	0.364
2	1.000	0.0638	15.681
3	0.490	0.0848	5.778
4	0.549	0.0590	9.300
5	0.751	0.1047	7.184
6	1.000	0.0605	16.529
7	1.000	0.1020	9.804

Table 3. Dataset "20221112150043_stare_HH.mat".

α	Target Response	Clutter Suppression	T-C Improvement
1	1.000	0.0177	56.381
2	1.000	0.0059	168.248
3	1.000	0.0060	166.506
4	1.000	0.0046	217.213
5	1.000	0.0069	145.460
6	1.000	0.0389	25.707
7	1.000	0.0511	19.565

6. Conclusions

This paper proposed a novel class of MIG detectors with MSP, which were specifically developed to address the critical challenge of target detection in nonhomogeneous sea clutter environments. After modeling the sample data as HPD matrices, we adopted an innovative manifold projection operation that mapped the original manifold onto an optimized discriminative submanifold. This projection not only amplified the geometric distance between target and clutter distributions but also inherently suppressed clutter interference, thereby providing an effective method for target detection in nonhomogeneous sea clutter, and offering a novel solution for radar target detection under complex sea conditions. We derived three MSP-MIG detectors incorporating different geometric measures: KLD, SKLD and LEM. Each variant captured unique aspects of manifold geometry, offering flexibility in balancing computational efficiency and detection sensitivity. Experimental results under both simulated and real sea clutter scenarios validated that the proposed MSP-MIG detectors consistently outperformed conventional MIG detectors without MSP, as well as classic adaptive detectors such as the ANMF. Notably, the MSP method demonstrated significant gains in detection probability under low SCRs and maintained robustness against clutter nonhomogeneity. In the future, the adaptive selection of the most suitable geometric measure (KLD, SKLD, LEM, etc.) based on real-time clutter characteristics remains an open and practical challenge, and we will continue our research to enhance the generalizability of the proposed method.

Author Contributions: Conceptualization and methodology, J.C., X.H. and Z.Y.; software, validation and data curation, J.C. and X.H.; formal analysis, Y.C. and H.W. (Hao Wu); investigation, J.C.; resources, X.H. and H.W. (Hongqiang Wang); writing—original draft preparation, J.C.; writing—review and editing, J.C. and X.H.; supervision, Y.C., Z.Y. and H.W. (Hongqiang Wang); project administration, X.H.; funding acquisition, X.H. and Z.Y. All authors have read and agreed to the published version of the manuscript.

Funding: This research was funded by the National Natural Science Foundation of China (Grant Nos. 62371458 and 62501616). The APC was funded by the National Natural Science Foundation of China (Grant No. 62371458).

Data Availability Statement: The datasets used in our real-data experiments are available online: (1) IPIX datasets: http://soma.ece.mcmaster.ca/ipix/grimsby/index.html, accessed on 5 February 2026. (2) The SDRDSP datasets: https://radars.ac.cn/web/data/getData?newsColumnId=67f99a4d-633c-4a60-8315-22d45e2c59e1, accessed on 5 February 2026.

Conflicts of Interest: The authors declare no conflicts of interest.

References

1. Guo, H.; Wu, H.; Wang, Z.; He, Z.; Cheng, Z. Adaptive Target Detection in Nonhomogeneous Clutter and Multipath Environment. *IEEE Trans. Aerosp. Electron. Syst.* **2025**, *4*, 9630–9644. [CrossRef]
2. Yu, H.; Cao, Z.; Wang, G.; Ding, H.; Liu, N.; Dong, Y. A Classification Method for Marine Surface Floating Small Targets and Ship Targets. *IEEE J. Miniaturization Air Space Syst.* **2024**, *5*, 94–99. [CrossRef]
3. Zheng, Q.; Yang, Y.; Xie, Y.; Li, J.; Hu, T.; Zhu, J. A Target Detection Scheme with Decreased Complexity and Enhanced Performance for Range-Doppler FMCW Radar. *IEEE Trans. Instrum. Meas.* **2021**, *70*, 1–13. [CrossRef]
4. Guan, T.; Chang, S.; Deng, Y.; Xue, F.; Wang, C.; Jia, X. Oriented SAR Ship Detection Based on Edge Deformable Convolution and Point Set Representation. *Remote Sens.* **2025**, *17*, 1612. [CrossRef]
5. Li, W.; Miao, Q.; Yuan, Y.; Tian, Y.; Yi, W.; Chan Teh, K. Automotive Radar Multi-Frame Track-Before-Detect Algorithm Considering Self-Positioning Errors. *IEEE Trans. Intell. Transp. Syst.* **2025**, *26*, 13506–13521. [CrossRef]
6. Chen, J.; Yi, C.; Gong, S.; Du, H.; Wu, W.; Kang, J.; Niyato, D. Generative AI-Aided QoE-Aware Resource Allocations for RIS-Assisted Digital Twin Interaction with Uncertain Evolution. *IEEE Trans. Mob. Comput.* **2025**, 1–18. [CrossRef]
7. Dong, Y.; Wei, J.; Ding, H.; Liu, N.; Cao, Z.; Yu, H. A Dynamic False Alarm Rate Control Method for Small Target Detection in Non-Stationary Sea Clutter. *J. Mar. Sci. Eng.* **2022**, *12*, 1770. [CrossRef]
8. Tan, Q.J.O.; Romero, R.A. Moving Target Detection and Classification with Dual-Matched Filter Discriminator for Coherent Jammer Suppression in Cognitive Radar. In Proceedings of the 2020 IEEE International Radar Conference, Washington, DC, USA, 28–30 April 2020; pp. 297–302.
9. Song, Y.; Pu, W.; Zhang, Y.; Zhang, Y. A Structure-Driven Multistage Trajectory Planning Method for BiSAR. *IEEE Trans. Geosci. Remote Sens.* **2025**, *63*, 2005114. [CrossRef]
10. Chen, J.; Shi, Y.; Yi, C.; Du, H.; Kang, J.; Niyato, D. Generative AI-Driven Human Digital Twin in IoT-Healthcare: A Comprehensive Survey. *IEEE Internet Things J.* **2024**, *11*, 34749–34773. [CrossRef]
11. Chen, Z.; Chen, A.; Liu, W.; Ma, X. CFAR Detection in Nonhomogeneous Weibull Sea Clutter for Skywave OTHR. *IEEE Geosci. Remote Sens. Lett.* **2023**, *20*, 3508005. [CrossRef]
12. Finn, H.M. Adaptive detection mode with threshold control as a function of spatially sampled clutter-level estimates. *RCA Rev.* **1968**, *25*, 414–465.
13. Trunk, G.V. Range resolution of targets using automatic detectors. *IEEE Trans. Aerosp. Electron. Syst.* **1978**, *5*, 750–755. [CrossRef]
14. Hansen, V.G. Constant false alarm rate processing in search radars. In *International Conference on Radar—Present and Future;* Institution of Electrical Engineers: London, UK, 1973; p. 325.
15. Conte, E.; Lops, M. Asymptotically optimum radar detection in compound Gaussian clutter. *IEEE Trans. Aerosp. Electron. Syst.* **1995**, *31*, 617–625. [CrossRef]
16. Conte, E.; Lops, M. Adaptive Detection Schemes in Compound-Gaussian Clutter. *IEEE Trans. Aerosp. Electron. Syst.* **1998**, *34*, 1058–1069. [CrossRef]
17. Liu, M.; Shui, P. Adaptive Matched Filter Detector Based on Power Median and Normalized Sample Covariance Matrix. *J. Electron. Inf. Technol.* **2015**, *6*, 1395–1401.
18. Rong, Y.; Aubry, A.; De Maio, A.; Tang, M. Adaptive Radar Detection in Low-Rank Heterogeneous Clutter via Invariance Theory. *IEEE Trans. Signal Process.* **2021**, *69*, 1492–1506. [CrossRef]
19. Liu, M.; Shui, P. Multichannel adaptive signal detection: Basic theory and literature review. *Sci. China Inf. Sci.* **2022**, *2*, 5–44. [CrossRef]
20. Xue, J.; Fan, Z.; Xu, S.; Pan, M. Persymmetric Adaptive Detection for Radar Targets in Compound Gaussian Clutter with Nakagami Texture. *IEEE Trans. Aerosp. Electron. Syst.* **2025**, *62*, 2292–2303. [CrossRef]
21. Alexandrov, C.; Draganov, A.; Kolev, N. An application of automatic target recognition in marine navigation. In Proceedings of the 1995 IEEE International Radar Conference, Alexandria, VA, USA, 8–11 May 1995; pp. 250–255.
22. Kim, J.; Lim, S.; Jung, J.; Kim, S. Two-Stage Clutter Suppression Method for Human Detection Using FMCW Radar. In Proceedings of the 2023 IEEE Radar Conference, San Antonio, TX, USA, 1–5 May 2023; pp. 1–6.

23. Xu, Z.; Wu, Q.; Ai, X.; Liu, X. Micromotion Frequency Estimation of Multiple Space Targets Based on RCD Spectrum. *IEEE Trans. Aerosp. Electron. Syst.* **2025**, *61*, 14019–14030. [CrossRef]
24. Liu, Y.; Li, C.; Fu, G. PJ-YOLO: Prior-Knowledge and Joint-Feature-Extraction Based YOLO for Infrared Ship Detection. *J. Mar. Sci. Eng.* **2025**, *13*, 226. [CrossRef]
25. Fan, Y.; Tao, M.; Su, J. Weak target detection based on joint fractal characteristics of autoregressive spectrum in sea clutter background. *IEEE Geosci. Remote Sens. Lett.* **2019**, *16*, 1824–1828. [CrossRef]
26. Yanovsky, F.; Prokopenko, I.; Rudiakova, A.; Rhee, H. Generalized Computer Model of Sea, Land and Atmospheric Clutter. In Proceedings of the 2022 23rd International Radar Symposium, Gdansk, Poland, 12–14 September 2022; pp. 431–436.
27. Tessema, S.H.; Bismor, D.; Wyżgolik, R. Advanced Signal Processing Techniques for Plasma-MAG Welding Process. In Proceedings of the 2024 Signal Processing: Algorithms, Architectures, Arrangements, and Applications, Poznan, Poland, 25–27 September 2024; pp. 188–193.
28. Wang, J.; Shi, K.; Li, S. Subband Two-Stage Collaborative Sea Clutter Suppression Based on Subregion Gazing and Reconstruction. *IEEE Geosci. Remote Sens. Lett.* **2024**, *21*, 1–5.
29. Li, J.; Li, Z.; Yang, Q. Efficient matrix sparse recovery STAP method based on kronecker transform for BiSAR sea clutter suppression. *IEEE Trans. Geosci. Remote Sens.* **2024**, *62*, 5103218. [CrossRef]
30. Liu, S.; Huang, D. Receptive field block net for accurate and fast object detection. In Proceedings of the 2018 Proceedings of the European Conference on Computer Vision, Munich, Germany, 8–14 September 2018; pp. 385–400.
31. De Maio, A.; Farina, A.; Foglia, G. Knowledge-Aided Bayesian Radar Detectors and Their Application to Live Data. *IEEE Trans. Aerosp. Electron. Syst.* **2010**, *46*, 170–183. [CrossRef]
32. Li, N.; Cui, G.; Yang, H.; Kong, L.; Liu, Q.H. Knowledge-aided Bayesian detection for MIMO radar in compound-Gaussian clutter with inverse Gamma texture. In Proceedings of the 2015 IEEE Radar Conference, Arlington, VA, USA, 27–30 October 2015; pp. 777–782.
33. Liu, X.; Li, Y.; Xu, S.; Du, L. Rao Test for Radar Target Detection in Sub-Gaussian Symmetric Alpha-Stable Sea Clutter. In Proceedings of the 2021 CIE International Conference on Radar, Haikou, China, 15–19 December 2021; pp. 1270–1273.
34. Gupta, M.; Chan, J.; Krouss, M.; Furlich, G.; Martens, P. Infrared Small Target Detection Enhancement Using a Lightweight Convolutional Neural Network. *IEEE Geosci. Remote Sens. Lett.* **2022**, *19*, 3513405. [CrossRef]
35. Chen, L.; Yang, Y.; Wang, Z.; Zhang, J.; Zhou, S.; Wu, L. Lightweight Underwater Target Detection Algorithm Based on Dynamic Sampling Transformer and Knowledge-Distillation Optimization. *J. Mar. Sci. Eng.* **2023**, *11*, 426. [CrossRef]
36. Feintuch, S.; Permuter, H.; Bilik, I.; Tabrikian, J. Neural Network-Based Multi-Target Detection within Correlated Heavy-Tailed Clutter. *IEEE Trans. Aerosp. Electron. Syst.* **2023**, *59*, 5684–5698. [CrossRef]
37. Zhang, X.; Gao, Y. Radar Target Detection Based on Convolutional Neural Network. *Comput. Meas. Control* **2021**, *2*, 49–52.
38. Pu, H. Research and Application on Object Detection Method based on Binary Neural Network. Ph.D. Thesis, Beijing Jiaotong University, Beijing, China, 2024.
39. Tian, Z.; Shen, C.; Chen, H. FCOS: A simple and strong anchor-free object detector. *IEEE Trans. Pattern Anal. Mach. Intell.* **2020**, *44*, 1922–1933. [CrossRef]
40. Do, T.; Kaddoum, G.; Nguyen, T. Multi-RIS-aided wireless systems: Statistical characterization and performance analysis. *IEEE Trans. Commun.* **2021**, *69*, 8641–8658. [CrossRef]
41. Soldera, J.; Alberto, C.; Scharcanski, J. Customized orthogonal locality preserving projections with soft-margin maximization for face recognition. *IEEE Trans. Instrum. Meas.* **2015**, *64*, 2417–2426. [CrossRef]
42. Moakher, M. On the averaging of symmetric positive-definite tensors. *J. Elast. Vol.* **2006**, *82*, 273–296. [CrossRef]
43. Xiong, J. Tangential Maneuvering Target Detection for Airborne Cognitive Radar. *IEEE Trans. Aerosp. Electron. Syst.* **2025**, *61*, 401–415. [CrossRef]
44. Grosdidier, S.; Baussard, A. Ship detection based on morphological component analysis of high-frequency surface wave radar images. *IET Radar Sonar Navig.* **2012**, *6*, 813–821. [CrossRef]
45. Sui, B. Simulation of Airborne Radar Sea Surface Scattering Based on Improved Sea Clutter Modeling. In Proceedings of the 2024 4th International Conference on Computer Science, Electronic Information Engineering and Intelligent Control Technology, Guangzhou, China, 8–10 November 2024; pp. 284–287.
46. Poisson, J.; Förster, J.; Böhler, C.O.; Gallus, M.; Ulland, A.; Biegel, G. Analysis of radar sea clutter data acquired during the MARLENE measurement campaign. In Proceedings of the 2016 IEEE International Symposium on Antennas and Propagation, Fajardo, PR, USA, 24–28 October 2016; pp. 2063–2064.
47. Yu, X.; Chen, X.; Huang, Y.; Zhang, L.; Guan, J.; He, Y. Radar Moving Target Detection in Clutter Background via Adaptive Dual-Threshold Sparse Fourier Transform. *IEEE Access* **2019**, *7*, 58200–58211. [CrossRef]
48. Zhang, T.; Zheng, W.; Cui, Z.; Zong, Y.; Li, C.; Zhou, X.; Yang, J. Sea-detecting radar experiment and target feature data acquisition for duDeep manifold-to-manifold transforming network for skeleton-based action recognition. *IEEE Trans. Multimed.* **2020**, *22*, 2926–2937.

49. Boumal, N. *An Introduction to Optimization on Smooth Manifolds*; Cambridge University Press: Cambridge, UK, 2023.
50. Tang, F.; Fan, M.; Tino, P. Generalized learning Riemannian space quantization: A case study on Riemannian manifold of SPD matrices. *IEEE Trans. Neural Netw. Learn. Syst.* **2021**, *32*, 281–292. [CrossRef]
51. Hua, X.; Ono, Y.; Peng, L.; Xu, Y. Unsupervised Learning Discriminative MIG Detectors in Nonhomogeneous Clutter. *IEEE Trans. Commun.* **2022**, *70*, 4107–4120. [CrossRef]
52. Chen, X.; Cheng, Y.; Wu, H.; Wang, H. Heterogeneous Clutter Suppression via Affine Transformation on Riemannian Manifold of HPD Matrices. *IEEE Trans. Geosci. Remote Sens.* **2022**, *60*, 5109813. [CrossRef]
53. Yang, Z.; Cheng, Y.; Wu, H.; Li, X.; Wang, H. Subband Information Geometry Detection Method Based on Orthogonal Projection for Weak Radar Targets. *J. Radars* **2023**, *12*, 776–792.
54. Iannazzo, B.; Porcelli, M. The riemannian barzilai–borwein method with nonmonotone line search and the matrix geometric mean computation. *IMA J. Numer. Anal.* **2018**, *38*, 495–517. [CrossRef]
55. Zhang, W.; Wu, D. Manifold embedded knowledge transfer for brain-computer interfaces. *IEEE Trans. Neural Syst. Rehabil. Eng.* **2020**, *28*, 1117–1127. [CrossRef] [PubMed]
56. Zhang, F.; Shi, Y.; Ng, H.K.T.; Wang, R. Information Geometry of Generalized Bayesian Prediction Using α-Divergences as Loss Functions. *IEEE Trans. Inf. Theory* **2018**, *64*, 1812–1824. [CrossRef]
57. Arnaudon, M.; Barbaresco, F.; Yang, L. Riemannian medians and means with applications to radar signal processing. *IEEE J. Sel. Top. Signal Process.* **2013**, *7*, 595–604. [CrossRef]
58. Hua, X.; Peng, L. MIG median detectors with manifold filter. *Signal Process.* **2021**, *188*, 108176. [CrossRef]
59. Chahrour, H.; Dansereau, R.M.; Rajan, S. Target detection through Riemannian geometric approach with application to drone detection. *IEEE Access* **2021**, *9*, 123950–123963. [CrossRef]
60. Yang, Z.; Cheng, Y.; Wu, H.; Yang, Y.; Qin, Y.; Wang, H.; Li, X. Enhanced matrix information geometry detection for weak targets in heterogeneous clutter environment. *Sci. China Inf. Sci.* **2025**, *11*, 387–388. [CrossRef]
61. Hua, X.; Peng, L.; Liu, W.; Cheng, Y.; Wang, H.; Sun, H.; Wang, Z. LDA-MIG Detectors for Maritime Targets in Nonhomogeneous Sea Clutter. *IEEE Trans. Geosci. Remote Sens.* **2023**, *61*, 5101815. [CrossRef]
62. Ashtiani, M.B.; Shahrtash, S.M. Partial discharge de-noising employing adaptive singular value decomposition. *IEEE Trans. Dielectr. Electr. Insul.* **2014**, *21*, 775–782. [CrossRef]
63. Kalantzis, V.; Traganitis, P.A. Rayleigh-Ritz Based Updates of the Multilinear Singular Value Decomposition. In Proceedings of the 2023 57th Asilomar Conference on Signals, Systems, and Computers, Pacific Grove, CA, USA, 29 October–1 November 2023; pp. 1059–1063.
64. Nazari, B.; Sarkrni, S.M.A.; Karimi, P. A method for noise reduction in speech signal based on singular value decomposition and genetic algorithm. In Proceedings of the IEEE EUROCON 2009, St. Petersburg, Russia, 18–23 May 2009; pp. 102–107.
65. Dixit, U.D.; Shirdhonkar, M.S. Logo based document image retrieval using singular value decomposition features. In Proceedings of the 2016 International Conference on Signal and Information Processing, Nanded, India, 6–8 October 2016; pp. 1–4.
66. Zhou, X.; Zhuang, J.; Yang, P.; Liu, B. Vibration displacement extraction method based on SVD decomposition and wavelet denoising. In Proceedings of the 2022 China Automation Congress, Xiamen, China, 25–27 November 2022; pp. 4386–4391.
67. Howland, P.; Park, H. Generalizing discriminant analysis using the generalized singular value decomposition. *IEEE Trans. Pattern Anal. Mach. Intell.* **2004**, *26*, 995–1006. [CrossRef] [PubMed]
68. Hua, X. Research on Radar Target Detection Method based on Matrix Information Geometry. Ph.D. Thesis, National University of Defense Technology, Changsha, China, 2018.
69. Hua, X.; Xu, C.; Wang, Z.; Liu, W. LDPP-MIG Detectors in Sample-Starved Nonhomogeneous Clutter. *IEEE Trans. Aerosp. Electron. Syst.* **2025**, *61*, 8695–8715. [CrossRef]
70. Liu, N.; Dong, Y.; Wang, G. Sea-detecting X-band radar and data acquisition program. *J. Radars* **2019**, *8*, 656–667.
71. Haykin, S. The McMaster IPIX Radar Sea Clutter Database. Available online: http://soma.ece.mcmaster.ca/ipix/index.html (accessed on 25 July 2025).
72. Ono, Y.; Peng, L. Towards a median signal detector through the total Bregman divergence and its robustness analysis. *Signal Process.* **2022**, *201*, 108728. [CrossRef]
73. Guan, J.; Liu, N.; Wang, G. Sea-detecting radar experiment and target feature data acquisition for dual polarization multistate scattering dataset of marine targets. *J. Radars* **2023**, *12*, 456–469.

Disclaimer/Publisher's Note: The statements, opinions and data contained in all publications are solely those of the individual author(s) and contributor(s) and not of MDPI and/or the editor(s). MDPI and/or the editor(s) disclaim responsibility for any injury to people or property resulting from any ideas, methods, instructions or products referred to in the content.